Crawling Soft Robot Exploiting Wheel-legs and Multimodal Locomotion for High Terrestrial Maneuverability

Xinpei Ai, Hengmao Yue, and Wei Dawid Wang*

***Abstract*—How to efficiently traverse complex terrain remains an unresolved challenge for mobile soft robots, because their deformable bodies limit the magnitude of the forces they can exert on the environment. To achieve high maneuverability, this study demonstrates a pneumatic soft crawling robot equipped with wheel-legs capable of multimodal locomotion to negotiate various obstacles. The soft robot consists of a pneumatic soft actuator capable of multiple modes of bending deformation as the body and four identical multi-spoked wheel-legs with passive unidirectional forward rotation as limbs. The synergy of the body actuator and wheel-legs enables the robot to achieve multiple crawling gaits, including gecko-like crawling and inchworm-like crawling. A single gait or a combination of multiple gaits, as well as shape-morphing of the body, enables the robot to navigate obstacles as diverse as confined spaces, inclined surfaces, gaps, and stairs, or to avoid obstacles by circumventing them. Our study substantially improves the maneuverability of pneumatic soft crawling robots, thereby providing new routes for the potential applications of soft robots in obstacle-filled scenarios, including search and rescue, exploration, and inspection.**

***Index Terms*—pneumatic soft robots, wheel-legs, multimodal locomotion, high mobility, obstacle traversal**

I. Introduction

The terrestrial environment is the primary habitat for a variety of animals. In order to traverse various types of terrain, animals have the capability of altering their locomotion dynamics to exhibit versatility and adaptability in locomotion [1]. Inspired by their biological counterparts, soft robots are designed to utilize the compliance and adaptability of soft materials and structures allowing for the embodied intelligence that can potentially reduce both the hardware and software complexities in ways not possible with conventional rigid robots [2]. Soft robots with simple structures can produce complex and continuous deformation through simple actuations, thereby various terrestrial locomotion, including crawling [3]–[5], walking [6]–[8], and rolling [9]–[11], can be accomplished to adapt to the cluttered and unstructured environment. A requirement for terrestrial motion is to be able to continuously negotiate different obstacles; however, it is still challenging for existing soft robots with fixed configurations to cross different obstacles, thus limiting their range of motion.

Terrestrial locomotion can be grouped into three basic forms: crawling (or limbless locomotion), legged locomotion, and wheeled locomotion (or rolling)[12]–[14]. These forms of locomotion can be realized by soft robots based on different actuation techniques such as including pneumatic soft actuators[15]–[22] and smart material-based soft actuators [23]–[28]. Among them, pneumatic soft actuators actuated by pressurized air are the most widely used, which can produce relatively high forces and deformations, and easily realize various modes of deformation through different distributions of pneumatic networks. Crawling locomotion, such as peristaltic, serpentine, and two anchor-based crawling, is achieved by periodic deformation of the robot body and employing differential friction between the robot body and the ground. It is because of this differential friction, provided by the inseparable contact surface between the robot and the ground, that these robots are generally restricted to moving on an even (and sometimes rough) surface, within a pipe, or along the outer surface of a beam[20]–[22], making it difficult for them to traverse diverse obstacles.

In addition, legs enable soft robots to generate more dexterous locomotion by the sequential actuation of multiple legs to better interact with different physical environments[6], [7]. However, due to their inherent softness, pneumatic soft robots cannot provide enough force to readily raise their legs to complete obstacle traversal[17]–[19]. In addition, legged locomotion provides discrete, rather than continuous motion on contact surfaces, which greatly affects stability when overcoming obstacles. To prevent falls, a simple strategy, without complex control methods, is to keep the soft robot's center of gravity in a balanced range at all times, but this also limits the robot's ability to overcome obstacles[29]–[31].

In contrast, wheels can provide efficient locomotion on almost even terrain, but they are limited in the type and size of obstacles that they can overcome as they exhibit low

This work was supported by the National Research Foundation of Korea (NRF) funded by the Korean government (MSIT) (No. RS-2023-00210231). (corresponding author: Wei Dawid Wang)

X. Ai, H. Yue, and W. Wang are with the Department of Mechanical Engineering, Hanyang University, Seoul, 04763, Republic of Korea (prime2333@hanyang.ac.kr; hengmaoyue@hanyang.ac.kr; davidwang@hanyang.ac.kr).

obstacle transverse capabilities. Especially when crossing a vertical obstacle, in general, the height of a vertical obstacle should not be higher than the radius of the wheel. To improve upon this limitation, wheel legs were introduced to robots to enable them to achieve locomotion that combines the speed and simplicity of wheels to move efficiently and the high mobility of legs to negotiate obstacles that would be too high for a wheel[32]–[35]. Similarly, the mobility and obstacle-crossing ability of soft robots are more likely to be improved by the introduction of wheel legs. However, few soft robots with wheel legs have been developed.

Animals, on the other hand, may perform different modes of locomotion and often transition between them to effectively traverse different media or overcome obstacles in complex environments. This has inspired many efforts to build soft locomotive robots with multi-model locomotion to offer unprecedented advantages to robot mobility. A combination of modes of locomotion allows robots to be capable of navigating through a greater variety of different obstacles or environments. Multimodal locomotion has been described in different pneumatic soft robotic systems [15]–[17], [19], however, they still struggle to traverse some obstacles, hindering their range of applications. This limitation is due to the softness of the robot itself and its inability to generate enough actuation force to overcome gravity while supporting and moving the body weight.

Here, this study blends the advantages of soft actuators, wheel-legs, and multimodal locomotion to construct a highly maneuverable soft crawling robot whose performance of obstacle traversal exceeds that of other existing soft crawling robots of the same scale (Figure 1). This design was accomplished by introducing wheel legs to a soft robot to enable the robot to be capable of multimodal locomotion for traversing or circumventing different obstacles. The robot consists of four wheel-legs with passive unidirectional forward rotation and one soft pneumatic actuator capable of multiple modes of bending deformations as the robot body. The synergy of the wheel-legs and body actuator enables the robot to achieve multiple crawling gaits, including gecko-like crawling and inchworm-like crawling. With multiple gaits, as well as various body deformations, the robot can navigate a variety of obstacles. The schematic models of different crawling gaits and obstacle traversal are summarized in Table AI.

II. Robot Design and Implementation

A. Design

The robot consists of four passive wheel-legs and a pneumatic soft body with the main dimensions shown in Figure 2A. The robot is symmetrically designed up and down to ensure that the robot can move in the same way once it has flipped. Each wheel leg has eight protruding spokes, and the number of spokes was determined to enable the robot to reach a relatively fast and stable speed but at the cost of sacrificing some obstacle-crossing ability (Fig. A1). The wheel was designed with a unidirectional forward rotation by introducing a ratchet mechanism where the wheel-leg and the gear of the ratchet are fixed on the same rotational shaft. This design results in a consistent rotational motion, and the pawl of the ratchet prevents their reverse rotation (Figure 2B). The pawl attaches its upper end to the gear by its gravity, and when the robot flips over, the paw can work in the same way. The gear rotates with the wheel so that the teeth of the gear and the upper tip of the pawl continuously collide, which may cause the pawl to rotate beyond its critical position, that is the position where its center of gravity is directly above its rotation axis. The pawl cannot return to its original position, which causes the pawl to no longer contact the teeth of the gear, thereby rendering the pawl ineffective. In addition, when the robot crawls on slopes or deforms its body in the vertical plane, the wheel legs will generate a pitch angle, which will make the pawl easier to deviate from its working position. A kinetic modeling of the motion of the pawl is established to describe the maximum rotational speed of the wheel-leg with different pitch angles that the pawl can withstand (Appendix C). Both experimental and modeling results indicate that the larger the pitch angle of the robot, the smaller the maximum rotational speed of the wheel that the pawl can withstand. For instance, the maximum rotation speeds of the wheels corresponding to the pitch angles of 0°, 30°, and 60° are 18.5, 14.2, and 8.6 rad/s respectively.

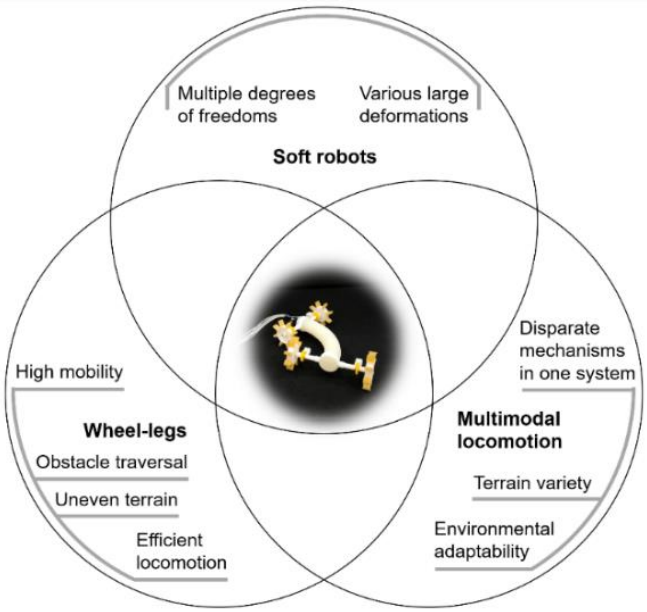

Fig. 1. Blending the advantages of soft robots, wheel-legs, and multimodal locomotion for high maneuverability. The soft actuators enable the robot to produce various large deformations and can thus be used in confined spaces. The wheel legs can improve the robot's ability to overcome obstacles, and the multi-modal locomotion allows the robot to adapt to different types of terrain. The combination of all three further enhances the robot's mobility.

The robot body was designed as a cylindrical shape with a pneumatic soft actuator composed of multiple pneumatic networks (PNs) embedded in the flexible elastomeric structures. To achieve a diversity of body deformations, the soft body was designed with six independent PNs parallel to the central long axis, and the cross-sectional area of all PNs is sector-shaped, a quarter-circle. There are two

axisymmetric PNs on the left and right sides (named PN-L and PN-R, indicated in purple), which run through the entire length of the actuator. In addition, there are two axisymmetric PNs up and down at the front (named PN-FU and PN-FD, in red) and rear sides (named PN-RU and PN-RD, in yellow), respectively, occupying the front half and the rear half of the actuator (Figure 2B). The vents of all the PNs are located at one end of the actuator determined as the rear end, and all the PNs were named based on their relative locations in the body actuator. Once the robot is flipped, the names of the PNs change accordingly.

Each PN consists of a series of connected chambers embedded in the extensible elastomer. All chambers with uniform gaps are oriented orthogonally to the long axis. The length of the left and right PNs is 101 mm, and the length of the other four PNs is 49 mm, all PNs start 4.5 mm from the nearest end of the body actuator. Pressurization of each PN inflates chambers to expand the top walls and stretch the inside walls, resulting in a bending deformation along the long axis of the actuator. The six PNs enable the body actuator to be capable of achieving various inflated configurations by pressurization of its PNs (Figure 2C). Upon pressurization, each PN curls to a final bending configuration at a rate that increases with the applied pressure. Figure 2E shows both experimental and modeling results for the bending curvature of the actuator based on a

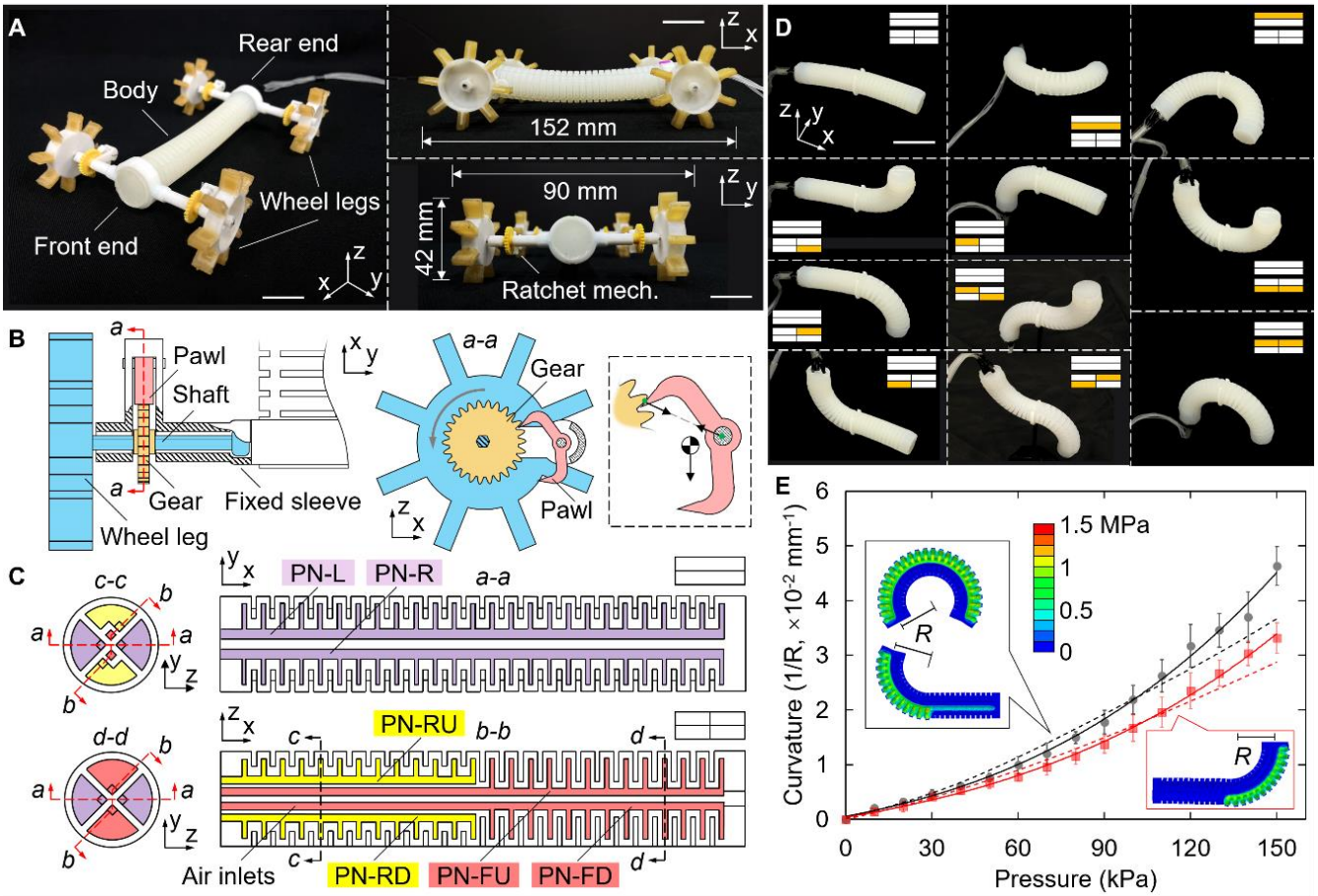

Fig. 2. Robot overview. (A) Robot profile. (B) Schematic of the wheel leg mechanism from the top view (left) and cut view (right). The inset shows that the pawl is in equilibrium subjected to two forces to prevent backward rotation of the gear. (C) Cross-sectional schematic diagrams of the soft body to show the six pneumatic PNs, including the left and right PNs (PN-L and PN-R), and the upper and lower PNs divided into the front and rear segments (PN-FU and PN-FD, PN-RU and PN-RD). The upper right insets show simplified diagrams of the six PNs. (D) Perspective views of the robot body in different configurations. The insets show schematic diagrams of the PNs where the pressurized and unpressurized PNs are indicated in orange and white, respectively. (E) Experimental (solid lines) and modeling (dash lines) results of the bending curvature of the body actuator by pressurization of one of its PNs. The black line represents the bending deformation of the actuator when one chamber of PN-L, PN-R, PN-FU, or PN-FD was pressurized, and the red line represents when one chamber of PN-RU or PN-RD was pressurized. The insets show the finite-element analysis of the von Mises stress distribution of the body actuator by pressurizing three different PNs at 150 kPa, with the labeled dimensions representing the radius of curvature. Scale bars: 40 mm.

different single PN. The PN-RU and PN-RD cause slightly smaller bending deformations due to the introduction of the air inlets making the cross-sectional area of these PNs slightly smaller than that of the other PNs. Experimental and modeling results show that moderate air pressure (such as 120 kPa) can enable the robot's body to obtain a large

deformation in the whole length (with around 180° in a length of 110 mm), and these results can also be used as a guide to quickly decide how much air pressure needs to be applied to obtain the desired deformation. In addition, the von Mises stress distribution of the body actuator at 150 kPa indicates that the actuator can well withstand the applied air pressure.

B. Materials and Fabrication

In this work, acrylonitrile butadiene styrene (ABS) is used to fabricate all the required rigid components, including the inner cores and outer molds, by 3D printing (Guider II S, Flashforge). The elastomer of Dragon Skin 20 (Smooth-On) is selected as the optimal material for constructing the robot's soft body, due to its high flexibility and reliability. In contrast to the selected elastomer, the implementation of a softer material in the robot's slender body would not only result in the undesired sagging of the abdomen to drag the ground but would also impede the provision of the necessary swing force, consequently causing a substantial decrease in crawling efficiency. Conversely, the utilization of a stiffer material presents challenges in achieving sufficient abdominal bending deformation, leading to a reduction in the crawling stride. The elastomer VytaFlex-10 (Smooth-On) is soft and can conform to micrometer-scale surface roughness, so it is chosen as the attachment material for the robot's wheel-legs to enhance the friction between them and the ground [36].

The fabrication process of the soft body actuator includes the following steps (Figure 3A). (*i*) The required inner cores and outer molds were first fabricated by 3D printing. Both ends of each inner core were designed with protrusions, and the outer mold reserves had corresponding notches for assembly. (*ii*) The inner cores and outer molds were assembled, and then Dragon Skin 20 (mixed 1A:1B by weight) was mixed, degassed using a vacuum pump to remove the bubbles generated during the mixing process, and poured to fill the assembly. (*iii*) The assembly was then covered with a top outer mold, and cured for four hours at room temperature. (*iv*) The outer molds were removed, and a cured semi-finished actuator was obtained. (*v*) The semi-finished actuator was immersed in acetone to dissolve the ABS inner cores to obtain the soft actuator. (*vi*) The soft actuator was rinsed and dried, and then the holes were filled at the front ends of the soft actuator with Dragon Skin 20. In addition, the six holes at the rear end of the soft actuator were connected with six flexible rubber tubes, and the seams between the tubes and the holes were sutured with silicone adhesive (Sil-poxy, Smooth-On). The fabrication of the wheel-leg is described in Figure 3B. An inner core and an outer mold were fabricated by using the same 3D printer. They were then assembled, and the assembly was filled using VytaFlex 10. The assembly was cured, and then the outer mold was removed to obtain the wheel leg. After fabrication of all components, the four wheel-legs were then installed to the soft body actuator through the ratchet mechanism to form the robot.

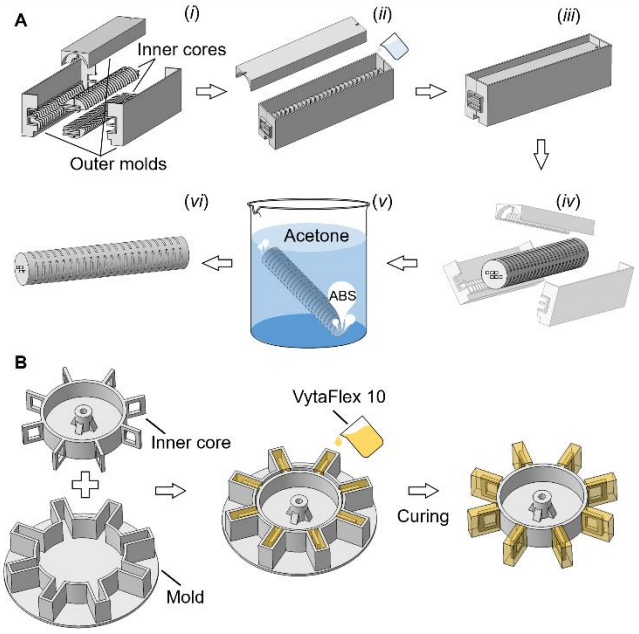

Fig. 3. Fabrication processes of the soft body actuator (A) and the wheel leg (B).

C. Performance evaluation of body actuator

The six air chambers of the robot are respectively controlled by six electro-pneumatic regulators (ITV003, SMC) connected to an air compressor. A microcontroller unit (MCU, Arduino Mega 2560) with a customized circuit was used to control the regulators to generate desired step inputs through the programs written on the MCU corresponding to the mentioned empirical crawling strategies for different obstacles. To verify the capability of the regulator to follow commanded pressures, the regulator was tested by inputting a step signal with the same 50% duty ratio but periods of 2, 3, 6, and 20 s, respectively. A pressure sensor (GZP168-102s, Sencoch) is connected to the outlet of the regulator to test the actual output air pressure. The results shown in Fig. A2 indicate that the response of the regulator to the signal is stable, but there will be a hysteresis response of 0.1s, and it takes about 1 s to reach the set air pressure (whether it is pressurization or depressurization). In addition, when the period is 2 s, although there is residual air pressure (about 6.5 kPa) in the air chamber when decompressing the chamber, this air pressure has a negligible effect on the deformation of the actuator. When the period increases to more than 3 s, the residual air pressure will not exist. Therefore, the shortest pressurization time of the step input for each air chamber of the robot was set as 1 s, so as to ensure that each air chamber of the robot can reach the set air pressure.

The robot contains six air chambers in three sets of symmetry. Experiments were conducted to test the reliability of the chambers with the effect of repeated sequential actuation on their deformation. To do so, one front half-length, one rear half-length, and one full-length air chamber were respectively actuated for 1000 cycles, each of which

was set for 3 s of pressurization with 150 kPa and 3 s of depressurization. One end of the actuator is fixed, and the displacement of the other end along the *y*-direction is tracked and recorded. The first 10 cycles and the last 10 cycles of 1000 cycles are plotted on the same graph shown in Fig. A3. One can see that, after 1000 cycles, the displacements of the three types of the chamber along the axial direction change by around 3.1, 0.9, and 4.3 mm, corresponding to an increase of 3.9%, 5.6%, and 8.5%, respectively. This increase is attributed to the certain plastic deformation of the air chamber after many times of actuation, resulting in an increase in the deformation of the actuator under the same air pressure. The same amount of deformation can be achieved by appropriately reducing the set air pressure for each chamber after prolonged actuation.

III. Results

A. Rectilinear motion with different gaits

By employing various bending deformations of the robot body, the friction between the wheel legs and the ground enables the wheel legs to rotate forward. The unidirectional rotation of the passive wheel legs then allows the robot to move only forward, and the sequential deformations of the body actuator allow the robot to exhibit multiple gaits of locomotion to suit different locomotion objectives. Two distinct gaits for the rectilinear motion are demonstrated based on the actuation pattern shown in Fig. A4. The first one is the gecko-like crawling gait, with a low center of gravity, achieved by alternately actuating the PN-L and PN-R (Figure 4A and 4B). Figure 4A shows a sequence of video frames depicting the forward gecko-like gait over a flat, level surface with a measured average stride of 155 mm in 2 s (more than one body length per stride), that is, 0.5 body lengths per second (BL/s). This robot can also perform an inchworm-like crawling gait by periodically pressurizing and depressurizing the upper PNs (PN-FU and PN-RU) simultaneously (Figure 4C and 4D). This gait is capable of accomplishing a measured average stride of 64 mm in 3 s (around 0.42 body lengths per stride), that is, 0.14 BL/s. The results show that the gecko-like gait can reach a higher speed than the inchworm-like gait. However, the gecko-like gait requires a wider operational workspace (around 1.4 times the body width) to accommodate the left and right swing of the robot body, compared to the inchworm-like gait, which only needs one body width. On the other hand, the inchworm-like gait requires more space in the vertical direction to accommodate the elevated body, compared to the gecko-like gait, which only needs a height greater than the outer diameter of the wheel-leg (Fig. A5, Movie S1).

B. Curvilinear motion with different gaits

Turning strategies are also illustrated based on the different actuation patterns of the PNs (Fig. A6). The first one, gecko-like turning, is conducted by periodically actuating only PN-R for left turns or PN-L for right turns. Figure 4F describes one stride for right-turning locomotion resulting in a turning speed of 20° per stride in 3 s, that is, 6.7° per second. The second one, inchworm-like turning, is achieved by periodically actuating PN-L, PN-FU, and PN-RU simultaneously for right turning, and the PNs of PN-R,

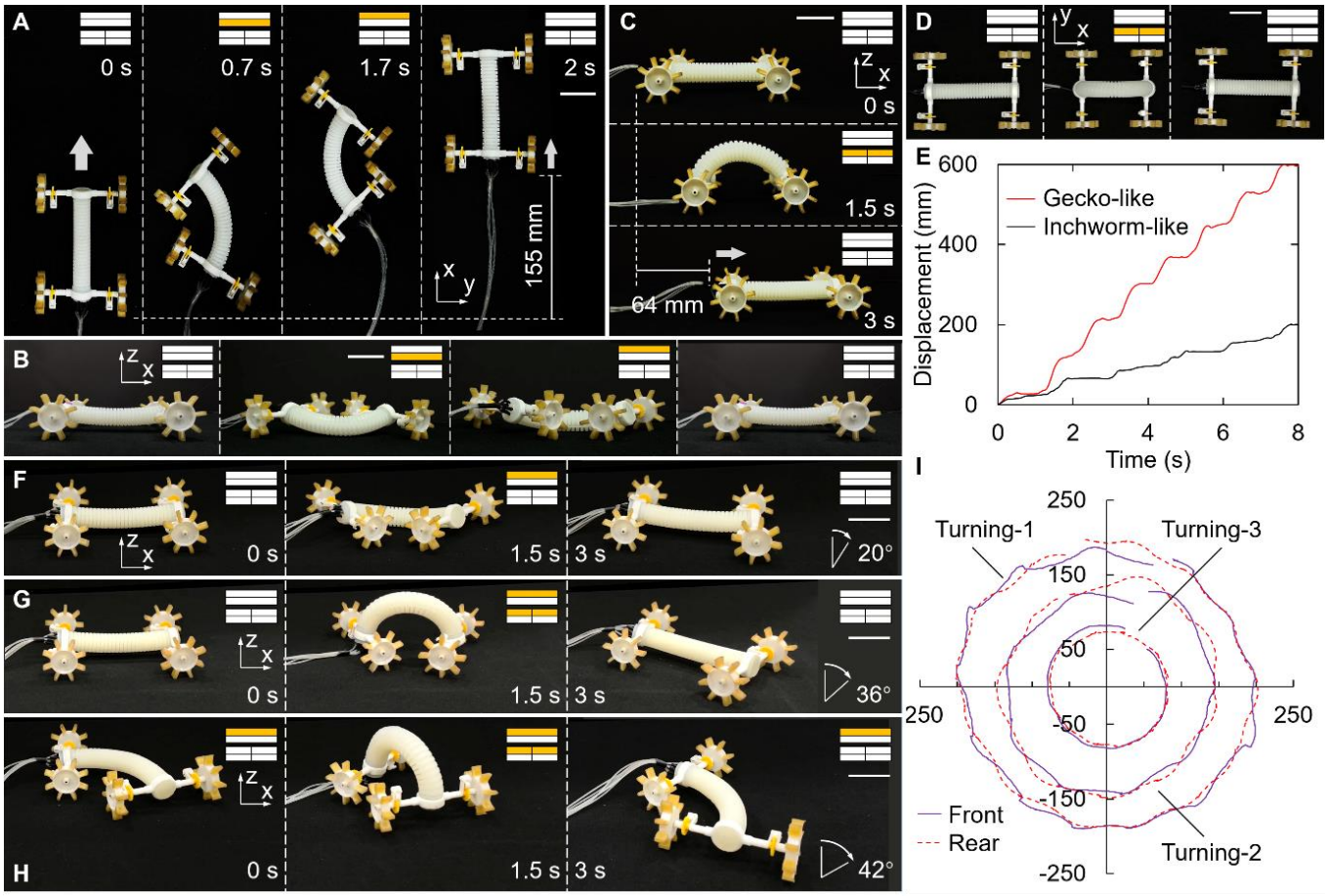

Fig. 4. Locomotion with different gaits. (A, B) Top view (A) and side view (B) of the gecko-like gait by alternately inflating the left and right PNs. (C, D) Top view (C) and side view (D) of the inchworm-like gait by inflating the two bottom pneumatic PNs simultaneously. The dotted lines mark the starting and finishing positions for one stride in (A) and (C). (E) The linear paths of the gecko-like and inchworm-like gait. Motion tracking software was used to track the markers at the front end of the robot. (F-H) The three turning modes. (I) 360-degree turning paths, by tracking the front and rear ends, based on three different turning modes. The orange blocks of the inserted schematic indicate the currently pressurized PNs; the white blocks indicate the unpressurized PNs. The time elapsed since the start of the gait is indicated in each figure.

PN-FU, and PN-RU simultaneously for left turning. Figure 4G describes one stride for right-turning locomotion resulting in a turning speed of 36° per stride in 3 s, that is, 12° per second. The third turning stride is achieved by first continuously actuating either PN-R or PN-L to bend the robot body to the right or left first, and then periodically actuating PN-FU and PN-RU. Figure 4H describes one stride for right-turning locomotion resulting in a turning speed of 42° per stride in 3 s, that is, 14° per second. The paths of a circular turn, obtained by tracking the front and rear ends of the robot, were completed in 54 s, 30 s, and 25.5 s, corresponding to around 18, 10, and 8.5 cycles, via the three different strategies, and the achieved turning radii were 200 mm, 150 mm, and 70 mm, respectively (Movie S2). It can be seen that the third turning strategy can achieve both the fastest turning speed and the minimum turning radius.

C. *Speed on different substrates*

The robot's speed is determined by the effective stride length which is sensitive to the resistant force from the substrate to the wheel-legs, which prevents them from sliding backward. Moreover, the amount of resistant force is mainly derived from the type of substrate. Further experiments were conducted to measure the robot speed on different substrates (Figure 5A). These experiments were conducted by enabling the robot, with the same applied actuation patterns to the PNs, to move on different horizontal surfaces, including a smooth acrylic plate, wet sand ground, gravel ground, grassland, and dry sand ground. The speed of the robot in two different motion modes, both gecko- and inchworm-like locomotion, was measured, and the results are shown in Figure 5B (Movie S3). The results show that the speed of the two crawling modes showed similar trends for different substrates, while the speed of the gecko-like mode was much higher than that of the inchworm. In addition, the results show that the robot runs faster on rigid and flat ground than on soft ground, and uneven ground also reduces the running speed of the robot due to resistance where the robot almost cannot move on gravel ground using an inchworm-like gait.

D. *Traversing diverse terrain: confined spaces*

The versatile locomotion of the robot can be exploited

to achieve fast motion over generally wide, open terrain using a gecko-like gait, whereas navigation through narrow passages can be approached using the inchworm-like gait, which operates within a body width (Movie S4). Figure 6A shows the robot crawling underneath an obstacle, i.e., an acrylic plate elevated 45 mm above the ground. The minimum passable elevated height should be greater than the diameter of the wheel legs (42 mm). Figure 6B shows the robot passing narrow passages with a minimum passable width of 90 mm (i.e., the width of the robot).

E. Traversing diverse terrain: inclined surfaces

The maximum slope angle that the robot can climb without slippage is theoretically determined by the coefficient of friction between the robot's wheel-legs and the ground. With a static coefficient of friction between the robot wheel leg (VytaFlex-10) and the acrylic surface of 2 [36], the maximum slope angle of the acrylic surface that the robot can climb is calculated as 63.4° (equals arctan2). Experiments were conducted on a flat, inclined acrylic surface to evaluate the climbing ability of the robot. Through experiments, a climbing angle of 55° was obtained for the gecko-like gait with a forward speed of 9.3 mm/s, and 30° for the inchworm-like gait with a forward speed of 4.6 mm/s, respectively (Fig. 6C, Movie S4). The inchworm-like gait has a lower climbing angle because it requires the robot to bulge its body, resulting in a larger slope angle at the rear end of the robot than the climbing angle, which can cause the ratchet mechanism of the rear wheel-legs to fail due to the separation of the paw and gear. This situation can be improved by only actuating the upper front half of the air channel (PN-FU) to be able to increase the maximum climbing angle to about 40° (Fig. A7). It can be seen that the maximum climbing angle of the gecko-like gait is always greater than that of the inchworm-like gait. This is because the gecko-like gait can maintain a lower center of gravity during climbing.

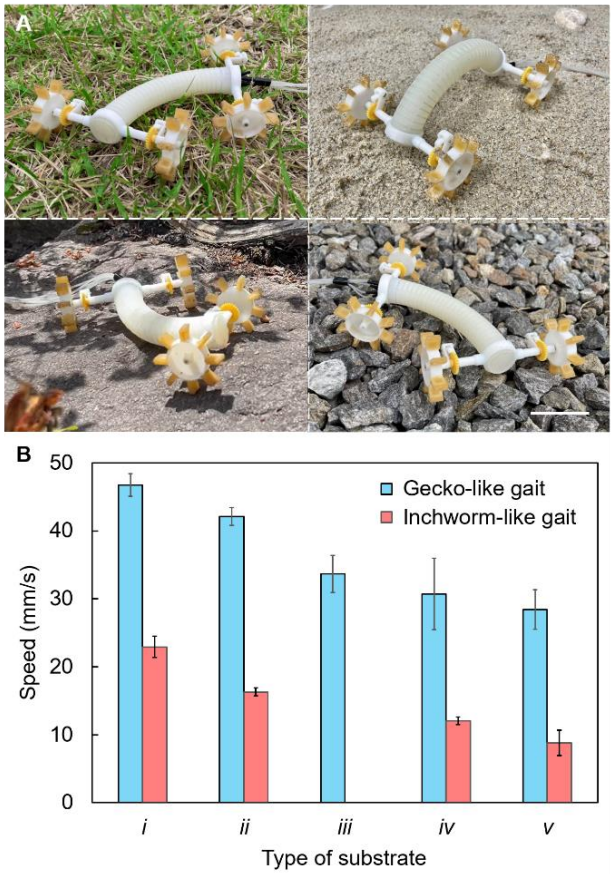

Fig. 5. Robot speed on different types of ground. (A) Images from experiments of the soft robot moving on a variety of grounds, including grassland, dry sand ground, rocky ground, and gravel ground. (B) Comparison of robot speed on different substrates: (*i*) a smooth acrylic plate, (*ii*) wet sand ground, (*iii*) gravel ground, (*iv*) grassland, and (*v*) dry sand ground. Scale bar: 40 mm.

F. Traversing diverse terrain: stairs

A combination of multiple crawling gaits, as well as various body morphing shapes, enables the robot to navigate more types of obstacles. To drive the robot to step over a stair (with a height greater than the wheel diameter), the sequence involves five basic steps from the resting position (Fig. 6D, Fig. A8). (*i*) Performing a crawling motion to enable the front end of the robot to be in contact with the stair. (ii) Pressurizing PN-FD to elevate the front end of the robot, and then pressurizing PN-L or PN-R to lift one of the two front wheel legs a little higher to touch the top edge of the stair. (iii) Performing one inchworm-like stride to get closer to the stair, and then pressurizing PN-FD to elevate the front end again to enable both the front wheel legs to touch the top edge of the stair. (iv) Performing inchworm-like strides to enable the two rear wheel legs/end to be in contact with the stair. (v) Applying a small amount of air pressure to the PN-RD to lift the rear end, and then performing a gecko-like gait to enable the rear end to climb the stair, afterward, depressurizing the PN-RD. A video of climbing a stair is available as Movie S5. Through trial and error, this control strategy enables the robot to be capable of climbing a stair with a maximum height of around 50 mm, which is 2.2 times the radius of the wheel leg.

G. *Traversing diverse terrain: gap-like obstacles*

The robot can also cross a gap with the sequence involving five basic steps from rest (Fig. 6E, Fig. A9). (*i*) Performing a crawling motion to enable the front end of the robot to approach the edge of the gap. (*ii*) Pressurizing PN-L (or PN-R) to push the wheel leg on the right (or left) side of the front end to enable it to cross the gap while at the same time applying a small amount of air pressure to PN-FD to lift the front end to prevent it from falling into the gap. (*iii*) Depressurizing PN-L (or PN-R) to straighten the body, and then pressurizing PN-FD to enable both front wheel legs to touch the opposite gap edge. (*iv*) Performing an inchworm-like gait to enable the rear end of the robot to approach the gap edge. (*v*) Applying a small amount of air pressure to PN-RD to lift the rear end, and then performing a gecko-like gait to enable the rear end to cross the gap, afterward, depressurizing PN-RD. A video of crossing the gap is available as Movie S6. Through trial and error, this control strategy enables the robot to be capable of crossing a gap with a maximum width of around 50 mm, which is 1.2 times the diameter of the wheel leg.

H. *Obstacle avoidance*

Additionally, the robots can exploit a variety of body deformations to avoid obstacles. Two strategies by turning or flipping the body are further described in which the robot can circumvent obstacles (Movie S7). The first one is shown in Figure 6F. It depicts the sequence of the robot raising its head by actuating the front bottom PN and then adjusting the orientation of the head by actuating the right or left PN, thereby changing the forward direction to the right or left. In addition, the robot can perform a reverse motion by flipping its body. Using a crawling gait, the robot is driven to the obstacle, raises its head, and then stands its body up and leans on the obstacle. Afterward, the robot bends outwards via actuating PN-FD and PN-RD to lean back, flips with the help of gravity, and then resumes the crawl gait to move in the reverse direction (Figure 6G). Figure 6H shows the manually controlled robot traversing a cluttered environment in a series of coherent movements, including avoiding obstacles, crossing a bump, and passing through a confined space (Movie S8).

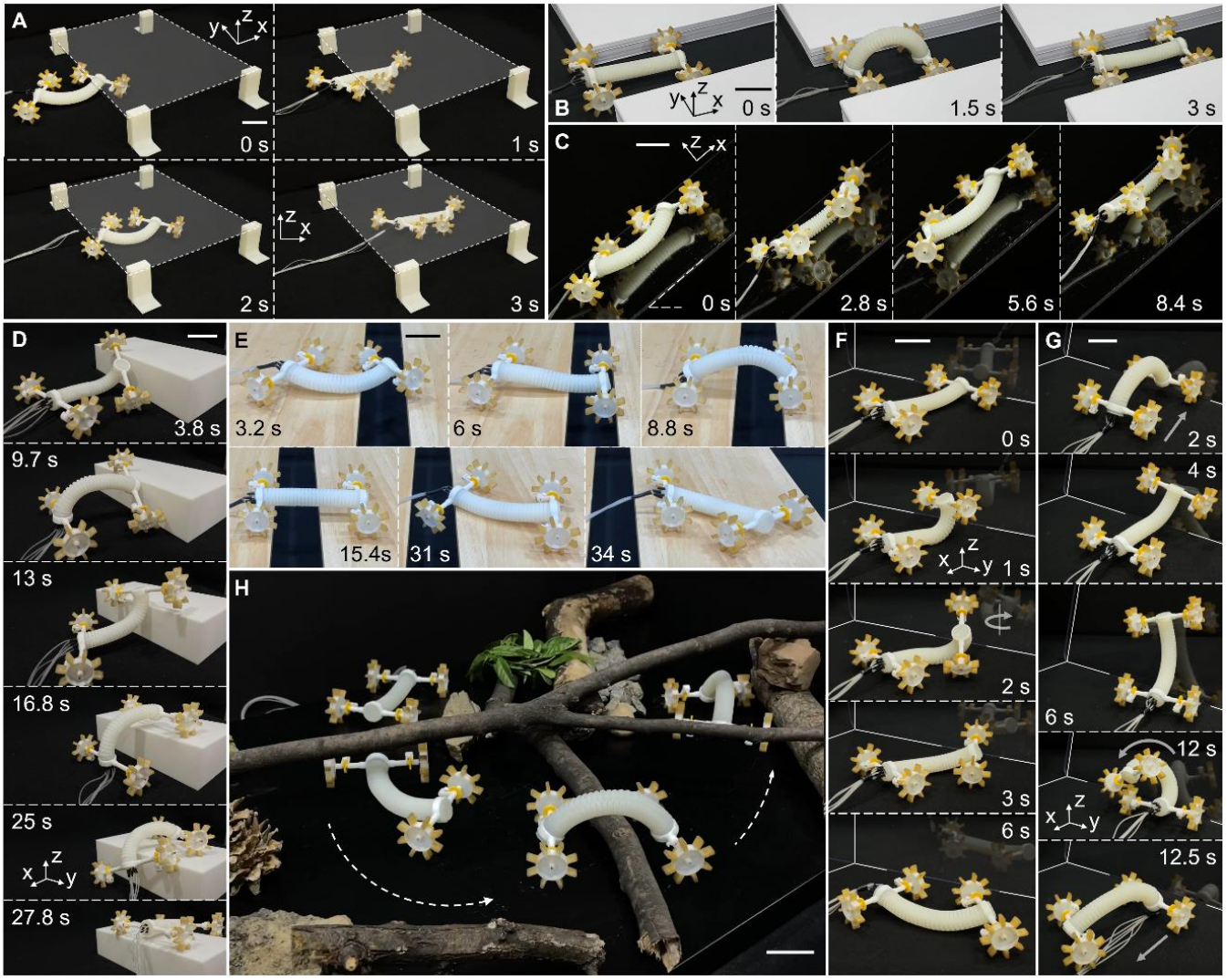

Fig. 6. Negotiating obstacles. (A) Crawling underneath an obstacle with a gecko-like gait. The shape of the obstacle is indicated by an overlaid dashed white line. (B) Passing through a narrow passage with an inchworm-like gait. (C) Crawling on a flat, inclined acrylic surface with gecko-like gaits. (D) Stepping over a stair with a combination of multiple gaits. (E) Crossing a gap obstacle. (F) Avoiding obstacles by changing the direction of motion. (G) Avoiding obstacles by flipping the body backward. (H) Traversing cluttered terrain. Scale bars: 40 mm.

TABLE I
PERFORMANCE COMPARISON OF DIFFERENT SOFT ROBOTS.

Soft robots	Actuation (body)	Actuation (limbs)	Weight (g)	Walking speed (BL/stride)	Turning speed (°/stride)	Slope angle (°)	Stair height (BH)	Gap width (BL)	Somersault ability	Terrain adaptability
Our robot	Pneumatic	Passive	48	1.02	42	55	1.1	0.5	Yes	Slopes, stairs, gaps, rough surfaces, hills, gravel, grassland, sand
Wu et al. [19]	N/A	Pneumatic	176	0.16	4.1	45	N/A	0.5	No	Smooth slopes, small hills, gaps, sand, water
Qin et al. [37]	Vacuum	Electroadhesive	43	0.12	30.2	90	N/A	0.15	No	Limited to smooth surfaces
Tang et al. [8]	Pneumatic	Passive	45	1.02	N/A	17	N/A	N/A	No	Limited to flat surfaces
Shepherd et al. [15]	Pneumatic	Pneumatic	N/A	0.17	N/A	N/A	N/A	N/A	No	Flat surfaces, low gaps
Hwang et al. [38]	SMA	Passive	29.9	0.09	5.03	N/A	N/A	N/A	No	Water, Smooth surfaces
Wang et al. [39]	SMA	Passive	63	0.03	2.3	N/A	N/A	N/A	No	Limited to smooth surfaces

Koh et al. [26]	SMA	Passive	1.2	0.06	7.9	N/A	N/A	N/A	No	Limited to smooth surfaces
Hu et al. [40]	DE	Electroadhesive	5	0.04	1.47	90	N/A	0.24	No	Walls, gaps, inverted surfaces
Gu et al. [41]	DE	Electroadhesive	12	0.045	3.14	90	N/A	N/A	No	Walls, low gaps

SMA: shape memory alloy, DE: dielectric elastomer.

IV. Conclusion

In summary, this study demonstrated a soft robot with excellent performance in all aspects as shown in Table I. The soft robot in this study can traverse different types of terrain, which is accomplished by introducing the wheel legs to a soft actuator with multiple modes of deformation to form a soft crawling robot capable of multimodal locomotion. The wheel legs were designed with unidirectional rotation, and the body actuator was designed to be capable of multiple modes of bending deformation, so that the robot can achieve two basic gaits, a gecko gait, and an inchworm gait. The gecko gait enables the robot to reach a speed of more than one body length per stride, around 78 mm/s. It is worth mentioning that the proposed soft robot is not limited to the crawling gaits described in this paper but could be used to generate more gaits. With a single crawling gait, the robot can travel through confined spaces with a minimum height equal to the diameter of the wheel-legs, pass through narrow passages with a minimum width equal to the width of the robot, and climb slopes with a maximum inclination of 55°. In addition, by virtue of a combination of multiple gaits as well as various body transformations, the robot can traverse or avoid a variety of obstacles. The robot can climb steps with a height equal to 2.2 times the radius of the wheel leg. The height of the steps that the proposed robot in its current configuration can climb was increased by 120% compared with a general wheeled robot, which can only climb steps with a height equal to the radius of the wheel. In addition, the robot can cross a gap with a width of 1.2 times the diameter of the robot's wheel. Furthermore, the robot can avoid obstacles that cannot be crossed by turning or flipping its body. Despite the remarkable adaptability of the robot to diverse environments, its current tethered operating system imposes limitations on its range of motion. Consequently, an untethered system will be needed to develop to expand the robot's range of motion, thereby facilitating a broader spectrum of operations. Additionally, visual-based autonomous navigation systems will be introduced to the robot to enable it to perform autonomous operations with minimal human intervention.

Appendix

A. Supplementary Table

TABLE AI
SCHEMATIC MODELS OF DIFFERENT CRAWLING GAITS AND OBSTACLE TRAVERSAL.

Gait types	Obstacle types	Schematic modeling	Key locomotion law	Description

Gecko-like gaits	--	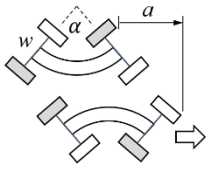	• Coefficient of friction $\mu \neq 0$. • Distance traveled per body swing (assuming no sliding) is $a = 2w\sin\left(\frac{1}{2}\alpha\right)$ where w and α are respective the robot width and the central angle corresponding to the lateral bending of the body.	• The back movement of a gecko-like gait uses lateral (side-to-side) undulations. • The one-way wheel produces friction difference between the front and rear wheel-legs (anchored wheel-legs are indicated in grey).
Inchworm-like gaits	--	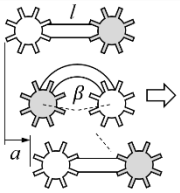	• Coefficient of friction $\mu \neq 0$. • Distance traveled per cycle (assuming no sliding) is $a = l - \frac{2l}{\beta}\sin\left(\frac{1}{2}\beta\right)$ where l and α are respective the robot length and the central angle corresponding to the vertical bending of the body.	• The back movement of an inchworm-like gait uses sagittal (up-and-down) movements. • One-way wheel produces front and rear friction difference (anchored wheel-legs are indicated in grey).
Gecko-like gaits or inchworm-like gaits	Confined spaces	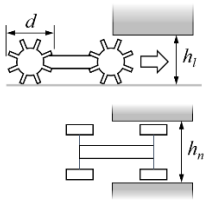	• Minimum $h_l = d$, where h_l and d are respective the height of the low gap and diameter of wheel-leg. • Minimum $h_n = w$, where h_n and w are respective the width of the narrow gap and with of the robot.	• The minimum height of the low gap that the robot can pass through should be higher than the height of the robot. • The minimum width of the narrow gap that the robot can pass through should be wider than the width of the robot.
Gecko-like gaits or inchworm-like gaits	Inclined surfaces	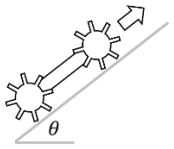	• The angle of inclination should be $\theta \leq \phi_s = \arctan\mu_s$, where θ, ϕ_s, and μ_s are respective the angle of inclination, the angle of static friction, and the static coefficient of friction. • The rotation speed of wheel $\omega_w \leq \omega_{\text{allow}}$, see Fig. A10.	• The slope should provide enough friction for the robot to prevent it from sliding down the slope. • The robot should have an appropriate movement speed to ensure the normal operation of the pawl.
Gecko-like gaits and inchworm-like gaits	Stairs	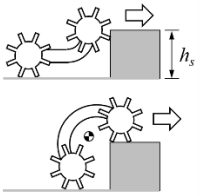	• CoG ∈ support polygon, then the highest height that can be crossed is $h_s = r + \frac{l}{\beta}\sin(\frac{1}{2}\beta)$	• To avoid falls, the center of gravity (CoG) should lay inside the support polygon.
Gecko-like gaits	Gaps	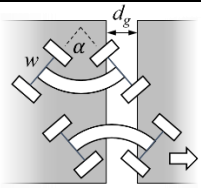	• The maximum width of the gap that the robot can cross is $h_g = w\sin(\frac{1}{2}\alpha)$	• The front axle swings with the body. When the two front wheels can touch both sides of the gap, the width of the gap can be simply regarded as the maximum width of the gap that the robot can span.
Gecko-like gaits and inchworm-like gaits	Body flipping	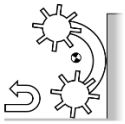	• CoG ∉ support polygon	• When the robot leans backward against the obstacle until its CoG is not within the support polygon, the robot can turn over to achieve reverse motion.

B. Supplementary Figures

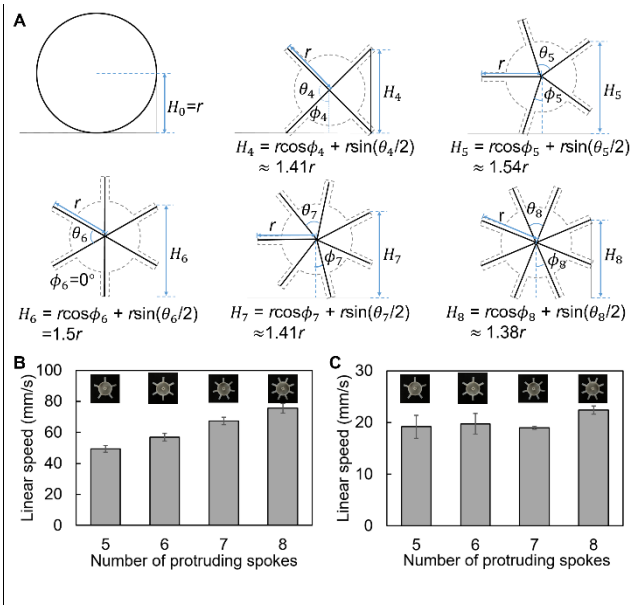

Fig. A1. Determination of the number of protruding spokes. (A) The theoretical maximum height of stairs that can be climbed by a wheel-leg with different numbers of protruding spokes. Assuming that the radius of the wheel leg is r, the stair heights that can be climbed by a wheel leg with zero, four, five, six, seven, and eight spokes are r, 1.41r, 1.54r, 1.5r, 1.41r, and 1.38r, respectively. (B) A robot designed with wheel-legs with five, six, seven, and eight spokes can reach a gecko-like crawling speed of 49.4, 56.9, 67.3, and 75.6 mm/s, respectively, based on the same actuation patterns of the PNs (that is, 120 and 120 kPa for PN-L and PN-R). (C) A robot designed with wheel-legs with five, six, seven, and eight spokes can reach a gecko-like crawling speed of 19.2, 19.7, 19.0, and 22.4 mm/s, respectively, based on the same actuation patterns of PNs (that is, 125 and 145 kPa for PN-FU and PN-RU). One can see from the results (B, C) that the wheel leg with eight spokes enables both the gecko-like gait and the inchworm-like gait to reach the maximum speed. Particularly in the case of the gecko-like locomotion, the linear speed of the wheel leg with eight spokes was increased by around 53%, 33%, and 12%, respectively, compared with that of the four, five, and six spokes. The number of spokes was determined to be eight to enable the robot to reach a relatively faster and more stable speed but at the cost of sacrificing some obstacle-crossing ability.

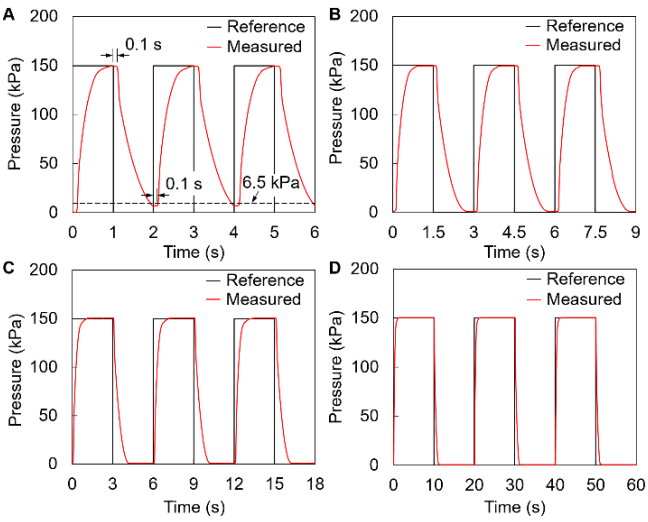

Fig. A2. Pressure response of the electro-pneumatic regulator by inputting step signals having the same 50% duty ratio, but with different periods of 2 (A), 3 (B), 6 (C), and 20 s (D), respectively.

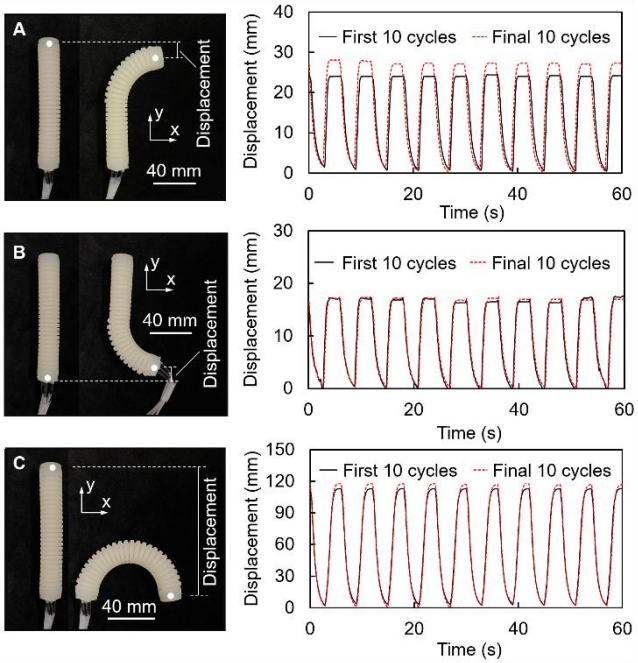

Fig. A3. Repeatability test of the body actuator through actuating one of the front half-length chambers (A), one of the rear half-length chambers (B), and one of the two full-length chambers (C), respectively.

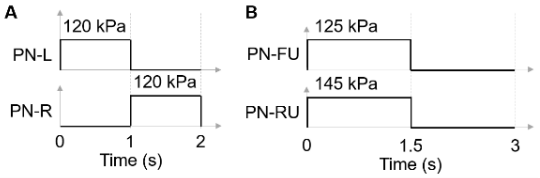

Fig. A4. Actuation patterns for rectilinear motion with different crawling gaits. (A) The gecko-like gait in one cycle (2 s). (B) The inchworm-like gait in one cycle (3 s).

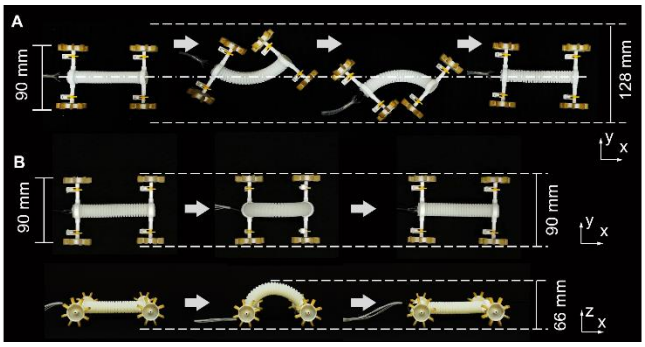

Fig. A5. Space required for the robot to achieve different gaits. (A) The gecko-like gait requires an operational workspace with a width of 128 mm, around 1.4 times the robot width, to accommodate the left and right swing of the robot body. (B) The inchworm-like gait requires a space with a height of 66 mm, around 1.6 times the diameter of the wheel leg, in the vertical direction to accommodate the elevated body.

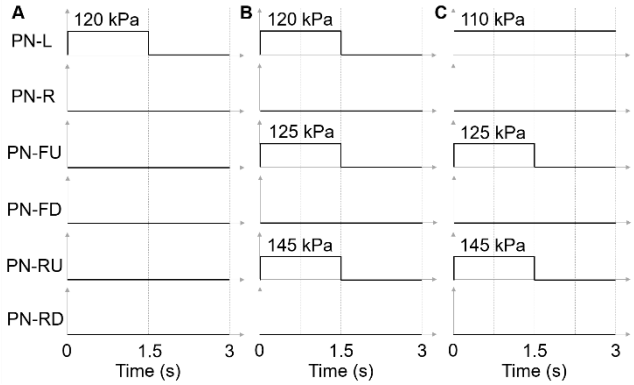

Fig. A6. Actuation patterns for curvilinear motion (right turning) with different crawling gaits. (A) Turning mode 1 in one cycle (3 s). (B) Turning mode 2 in one cycle (3 s). (C) Turning mode 3 in one cycle (3 s).

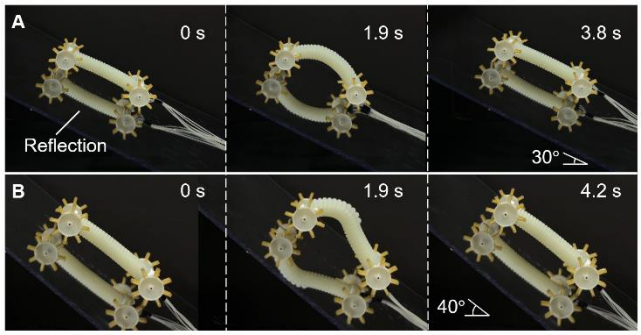

Fig. A7. Climbing slopes using the inchworm gait. The climbing ability of the robot using an inchworm-like gait was further evaluated on a flat, inclined acrylic surface by actuating the upper front and upper rear half-length chambers (A) or by only actuating the upper front half-length chamber (B). The maximum climbing angle can be improved by only actuating the upper front half of the air channel to reach a larger climbing angle of about 40°.

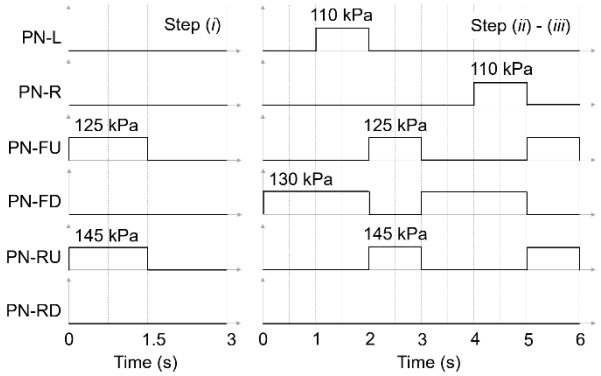

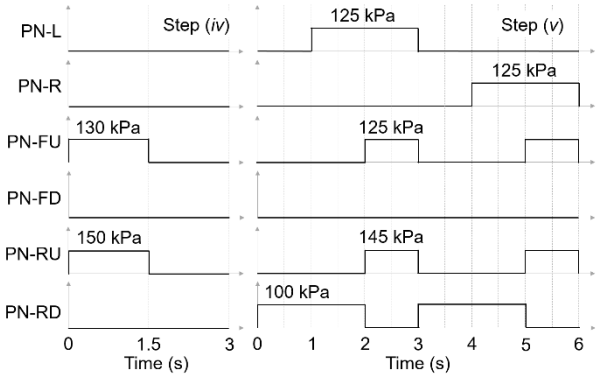

Fig. A8. Actuation patterns for traversing a stair.

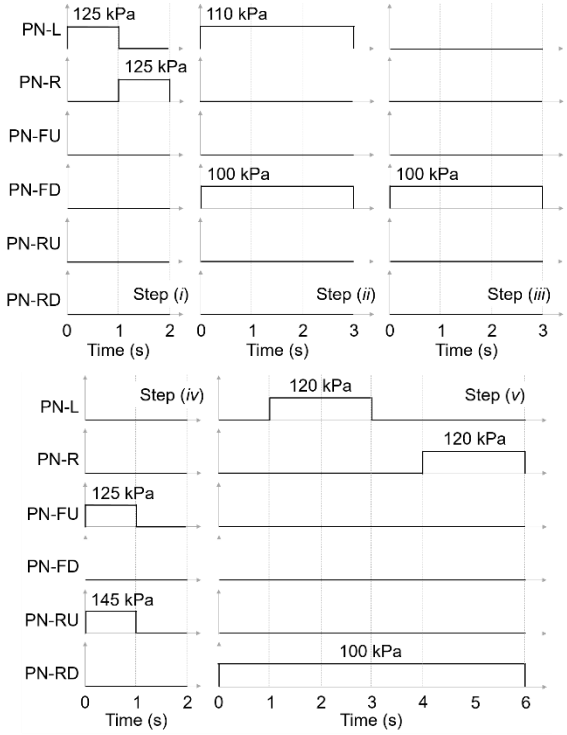

Fig. A9. Actuation patterns for traversing a gap-like obstacle.

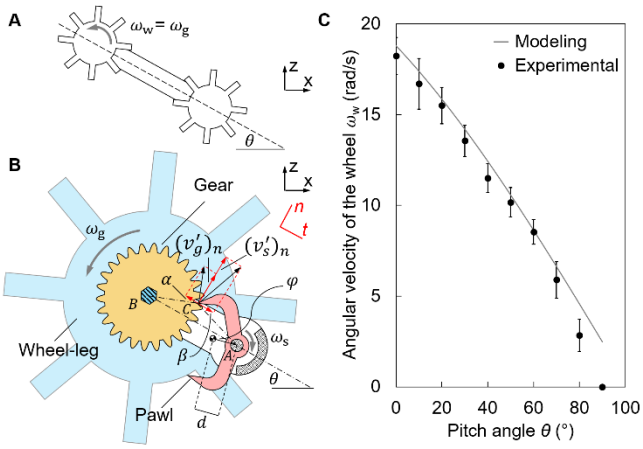

Fig. A10. Kinetic analysis of the failure of the pawl. (A) The robot with a pitch angle of θ. (B) Velocity analysis of the pawl and the gear for either the front or rear wheel-leg. (C) The maximum rotational speed of the wheel-

leg that the pawl can withstand when the robot was placed at different pitch angles.

C. Kinetic analysis of the pawl

The rotation of the gear that rotates coaxially with the wheel-leg causes the teeth of the gear to successively collide with the upper tip of the pawl. The collision enables the pawl to generate a rotation speed and associated kinetic energy. The kinetic energy will enable the pawl to move away from its original position, or even to cross its critical position, that is, the position where its center of gravity is directly above its rotation axis, and cannot return to the original position, thereby rendering the pawl non-functional. Therefore, the kinetic analysis of the motion of the pawl is established to describe the maximum rotational speed of the wheel-leg that the pawl can withstand when the robot moves on different slopes.

Assuming that the robot has a pitch angle θ varying from 0° to 90°, it is equivalent to the robot being placed on an inclined plane. The kinematic analysis of the velocities of the gear and the pawl is shown in Fig. A10. The gear and the pawl collide at point *C*, and coordinate axes are determined as the *n*-axis along the line of impact and the *t*-axis along their common tangent. Then the relation between the relative velocities of the two corresponding collision points on the gear and pawl along the line of impact can be

$$(v'_S)_n-(v'_g)_n=e[(v_g)_n-(v_S)_n] \tag{1}$$

where $(v_g)_n$ and $(v_S)_n$ represent the velocity components in the *n*-axis before the collision at points on the gear and the pawl coincident with the collision point *C*, and $(v'_g)_n$ and $(v'_g)_n$ represent their velocity components in the same direction just after the collision, respectively. Assuming the collision is a perfectly elastic impact, the coefficient of restitution *e* between the two bodies equals 1. In addition, because the mass of the gear associated with the wheel-leg (3.9 g) is much greater than that of the pawl (m=0.1 g), we can assume that $(v_g)_n=(v'_g)_n$ and $(v_S)_n$ is approximately 0. Then the angular velocity of the gear ω_g and that of the pawl ω_S can be determined as

$$\begin{aligned}\omega_g &= \frac{(v'_g)_n}{r_g\cos\alpha}\\ \omega_S &= \frac{(v'_S)_n}{r_S\cos\beta}\end{aligned} \tag{2}$$

where r_g and r_S represent the distances from *C* to the rotation axis of the gear and the pawl, respectively; α and β represent the angles between line *BC* and the *t*-axis, line *AC* and the *t*-axis, respectively. Then, the kinetic energy of the pawl *T* about its rotation axis just after the collision is

$$T=\frac{1}{2}I\omega_S^2 \tag{3}$$

where I represents the mass moment of inertia of the pawl. The work done by the gravitational force of the pawl to reach its critical position should be

$$V=mgd[1+\sin(\varphi-\theta)] \tag{4}$$

where d represents the distance between the mass center of the pawl and its rotation axis, φ represents the inclination angle of the pawl when it collides with the gear, that is, the angle between the line of symmetry of the pawl and the line *AB*. Assuming the friction of the rotation axis of the pawl is negligible, the mechanical energy of the pawl from the position just after the collision to its critical position is conserved. Therefore, it should be ensured that T is less than V so that the pawl cannot cross its critical position, and keep the pawl in working condition. The parameters that can be directly measured from a CAD model (via CATIA V5) are α, β, φ, r_g, r_S, d, and I, and their corresponding values are 20.2°, 38.9°, 11.8°, 7.0 mm, 7.4 mm, 1.6 mm, and 2.0 g·mm^2, respectively. Experiments were also conducted by using a motor to rotate the wheel with different pitch angles. Both experimental and modeling results shown in Fig. A10 indicate that the larger the pitch angle of the robot, the smaller the maximum rotational speed of the wheel that the pawl can withstand.

REFERENCES

[1] R. J. Lock, S. C. Burgess, and R. Vaidyanathan, "Multi-modal locomotion: From animal to application," *Bioinspiration and Biomimetics*, vol. 9, p. 011001, 2014, doi: 10.1088/1748-3182/9/1/011001.

[2] S. Coyle, C. Majidi, P. LeDuc, and K. J. Hsia, "Bio-inspired soft robotics: Material selection, actuation, and design," *Extrem. Mech. Lett.*, vol. 22, pp. 51–59, 2018, doi: 10.1016/j.eml.2018.05.003.

[3] W. Wang, J.-Y. Lee, H. Rodrigue, S.-H. Song, W.-S. Chu, and S.-H. Ahn, "Locomotion of inchworm-inspired robot made of smart soft composite (SSC)," *Bioinspir. Biomim.*, vol. 9, no. 4, p. 046006, Jan. 2014, doi: 10.1088/1748-3182/9/4/046006.

[4] M. S. Verma, A. Ainla, D. Yang, D. Harburg, and G. M. Whitesides, "A Soft Tube-Climbing Robot," *Soft Robot.*, vol. 5, no. 2, pp. 133–137, 2018, doi: 10.1089/soro.2016.0078.

[5] M. A. Bell, J. C. Weaver, and R. J. Wood, "An Ambidextrous STarfish-Inspired Exploration and Reconnaissance Robot (The ASTER-bot)," *Soft Robot.*, vol. Online, p. https://doi.org/10.1089/soro.2021.0053, 2021, doi: 10.1089/soro.2021.0053.

[6] A. Nemiroski *et al.*, "Arthrobots," *Soft Robot.*, vol. 4, no. 3, pp. 183–190, 2017, doi: 10.1089/soro.2016.0043.

[7] D. Drotman, S. Jadhav, D. Sharp, C. Chan, and M. T. Tolley, "Electronics-free pneumatic circuits for controlling soft-legged robots," *Sci. Robot.*, vol. 6, no. 51, p. eaay2627, 2021, [Online]. Available: https://robotics.sciencemag.org/lookup/doi/10.1126/scirobotics.aay2627.

[8] Y. Tang *et al.*, "Leveraging elastic instabilities for amplified performance: Spine-inspired high-speed and high-force soft robots," *Sci. Adv.*, vol. 6, no. 19, 2020, doi: 10.1126/sciadv.aaz6912.

[9] H.-T. Lin, G. G. Leisk, and B. Trimmer, "GoQBot: a caterpillar-inspired soft-bodied rolling robot," *Bioinspir. Biomim.*, vol. 6, no. 2, p. 026007, 2011, doi: 10.1088/1748-3182/6/2/026007.

[10] Y. C. Cheng, H. C. Lu, X. Lee, H. Zeng, and A. Priimagi, "Kirigami-Based Light-Induced Shape-Morphing and Locomotion," *Adv. Mater.*, vol. 32, no. 7, p. 1906233, 2020, doi:

10.1002/adma.201906233.
[11] J. J. Wie, M. R. Shankar, and T. J. White, "Photomotility of polymers," *Nat. Commun.*, vol. 7, p. 13260, 2016, doi: 10.1038/ncomms13260.
[12] F. Cotta, F. Icardi, G. T. Zurlo, and R. M. Molfino, "Peristaltic locomotion: Application to a worm-like Robot," *Proc. 8th Int. Conf. Climbing Walk. Robot. Support Technol. Mob. Mach. CLAWAR 2005*, pp. 501–508, 2006, doi: 10.1007/3-540-26415-9_60.
[13] M. Calisti, G. Picardi, and C. Laschi, "Fundamentals of soft robot locomotion," *J. R. Soc. Interface*, vol. 14, no. 130, 2017, [Online]. Available: http://rsif.royalsocietypublishing.org/content/14/130/20170101?cpetoc.
[14] C. S. X. Ng, M. W. M. Tan, C. Xu, Z. Yang, P. S. Lee, and G. Z. Lum, "Locomotion of Miniature Soft Robots," *Adv. Mater.*, vol. 33, no. 19, p. 2003558, 2020, doi: 10.1002/adma.202003558.
[15] R. F. Shepherd *et al.*, "Multigait soft robot," *Proc. Natl. Acad. Sci. U. S. A.*, vol. 108, no. 51, pp. 20400–20403, 2011, doi: 10.1073/pnas.1116564108.
[16] W. K. Lee *et al.*, "A buckling-sheet ring oscillator for electronics-free, multimodal locomotion," *Sci. Robot.*, vol. 7, no. 63, p. eabg5812, 2022, doi: 10.1126/scirobotics.abg5812.
[17] M. A. Robertson and J. Paik, "New soft robots really suck : Vacuum-powered systems empower diverse capabilities," *Sci. Robot.*, vol. 2, no. 9, p. eaan6357, 2017.
[18] M. T. Tolley *et al.*, "A Resilient, Untethered Soft Robot," *Soft Robot.*, vol. 1, no. 3, pp. 213–223, Sep. 2014, doi: 10.1089/soro.2014.0008.
[19] M. Wu *et al.*, "A Fully 3D-Printed Tortoise-Inspired Soft Robot with Terrains-Adaptive and Amphibious Landing Capabilities," *Adv. Mater. Technol.*, vol. Online, p. 2200536, 2022, doi: 10.1002/admt.202200536.
[20] A. Rafsanjani, Y. Zhang, B. Liu, S. M. Rubinstein, and K. Bertoldi, "Kirigami skins make a simple soft actuator crawl," *Sci. Robot.*, vol. 3, no. 15, p. eaar7555, 2018, doi: 10.1126/scirobotics.aar7555.
[21] H. Yang, S. Jin, and W. D. Wang, "Modular Assembly of Soft Machines via Multidirectional Reclosable Fasteners," *Adv. Intell. Syst.*, vol. 2200048, 2022, doi: 10.1002/aisy.202200048.
[22] T. Jin *et al.*, "Origami-Inspired Soft Actuators for Stimulus Perception and Crawling Robot Applications," *IEEE Trans. Robot.*, vol. 38, no. 2, pp. 748–764, 2022, doi: 10.1109/TRO.2021.3096644.
[23] W. Hu, G. Z. Lum, M. Mastrangeli, and M. Sitti, "Small-scale soft-bodied robot with multimodal locomotion," *Nature*, pp. 1–5, 2018, doi: 10.1038/nature25443.
[24] Q. Ze *et al.*, "Spinning-enabled wireless amphibious origami millirobot," *Nat. Commun.*, vol. 13, p. 3118, 2022, doi: 10.1038/s41467-022-30802-w.
[25] Y. Kim, G. A. Parada, S. Liu, and X. Zhao, "Ferromagnetic soft continuum robots," *Sci. Robot.*, vol. 4, p. eaax7329, 2019.
[26] J. S. Koh and K. J. Cho, "Omega-shaped inchworm-inspired crawling robot with large-index-and-pitch (LIP) SMA spring actuators," *IEEE/ASME Trans. Mechatronics*, vol. 18, no. 2, pp. 419–429, 2013, doi: 10.1109/TMECH.2012.2211033.
[27] J. Guo, C. Xiang, A. Conn, and J. Rossiter, "All-Soft Skin-Like Structures for Robotic Locomotion and Transportation," *Soft Robot.*, vol. 7, no. 3, pp. 309–320, 2020, doi: 10.1089/soro.2019.0059.
[28] S. Palagi *et al.*, "Structured light enables biomimetic swimming and versatile locomotion of photoresponsive soft microrobots," *Nat. Mater.*, vol. 15, no. February, pp. 1–8, 2016, doi: 10.1038/nmat4569.
[29] Q. Zhao, Y. Wang, H. Cui, and X. Du, "Bio-inspired sensing and actuating materials," *J. Mater. Chem. C*, vol. 7, no. 22, pp. 6493–6511, 2019, doi: 10.1039/c9tc01483g.
[30] X. Ji *et al.*, "An autonomous untethered fast soft robotic insect driven by low-voltage dielectric elastomer actuators," *Sci. Robot.*, vol. 4, no. 37, 2019, doi: 10.1126/scirobotics.aaz6451.
[31] Q. He, Z. Wang, Y. Wang, A. Minori, M. T. Tolley, and S. Cai, "Electrically controlled liquid crystal elastomer-based soft tubular actuator with multimodal actuation," *Sci. Adv.*, vol. 5, no. 10, p. eaax5746, 2019, doi: 10.1126/sciadv.aax5746.
[32] Y. S. Kim, G. P. Jung, H. Kim, K. J. Cho, and C. N. Chu, "Wheel Transformer: A wheel-leg hybrid robot with passive transformable wheels," *IEEE Trans. Robot.*, vol. 30, no. 6, pp. 1487–1498, 2014, doi: 10.1109/TRO.2014.2365651.
[33] S. C. Chen, K. J. Huang, W. H. Chen, S. Y. Shen, C. H. Li, and P. C. Lin, "Quattroped: A leg-wheel transformable robot," *IEEE/ASME Trans. Mechatronics*, vol. 19, no. 2, pp. 730–742, 2014, doi: 10.1109/TMECH.2013.2253615.
[34] C. Li, T. Zhang, and D. I. Goldman, "A terradynamics of legged locomotion on granular media," *Science (80-.).*, vol. 339, no. 6126, pp. 1408–1412, 2013, doi: 10.1126/science.1229163.
[35] L. Yehezkel, S. Berman, and D. Zarrouk, "Overcoming Obstacles with a Reconfigurable Robot Using Reinforcement Learning," *IEEE Access*, vol. 8, pp. 1–1, 2020, doi: 10.1109/access.2020.3040896.
[36] O. Unver and M. Sitti, "Flat dry elastomer adhesives as attachment materials for climbing robots," *IEEE Trans. Robot.*, vol. 26, no. 1, pp. 131–141, 2010, doi: 10.1109/TRO.2009.2033628.
[37] J. Z. Lei Qin, Xinquan Liang, Hui Huang, Chee Kong Chui, Raye Chen-Hua Yeow, "A Versatile Soft Crawling Robot with Rapid Locomotion," *Soft Robot.*, vol. 6, no. 4, pp. 455–467, 2019.
[38] J. Hwang and W. D. Wang, "Shape Memory Alloy-Based Soft Amphibious Robot Capable of Seal-Inspired Locomotion," *Adv. Mater. Technol.*, p. DOI: 10.1002/admt.202101271, 2022, doi: 10.1002/admt.202101153.
[39] W. Wang, J.-Y. Lee, H. Rodrigue, S.-H. Song, W.-S. Chu, and S.-H. Ahn, "Locomotion of inchworm-inspired robot made of smart soft composite (SSC)," *Bioinspir. Biomim.*, vol. 9, no. 4, p. 046006, Oct. 2014, doi: 10.1088/1748-3182/9/4/046006.
[40] J. L. Tete Hu, Xinjiang Lu, "Inchworm-Like Soft Robot with Multimodal Locomotion Using an Acrylic Stick-Constrained Dielectric Elastomer Actuator," *Adv. Intell. Syst.*, vol. 5, p. 2200209, 2023.
[41] G. Gu, J. Zou, R. Zhao, X. Zhao, and X. Zhu, "Soft wall-climbing robots," *Sci. Robot.*, vol. 3, p. eaat2874, 2018, doi: 10.1126/scirobotics.aat2874.

Xinpei Ai received the B.S. and M.S. degrees from the Department of Mechanical Engineering, Hanyang University, Korea, in 2021 and 2023. His research interests include soft robotics and bioinspired robots.

Hengmao Yue received the M.S. degree from the School of Astronautics, Beihang University, Beijing, China, in 2019. He is currently a Ph.D. candidate in Mechanical Engineering, Hanyang University, Korea. His research interests include soft robotics and bioinspired robots.

Wei Dawid Wang received the B.S. and M.S. degrees from the School of Mechatronics Engineering, Harbin Institute of Technology, China, in 2008 and 2011, and the Ph.D. degree from the Department of Mechanical Engineering, Seoul National University, Korea, in 2016. He is currently an Assistant Professor of Mechanical Engineering at Hanyang University. His research interests include soft robotics, bioinspired robots, and smart materials & structures.